

Institut für Angewandte Physik
der Universität Bonn

Wegelerstraße 8
53115 Bonn

A Magnetic Elevator for Neutral Atoms into a 2D State-dependent Optical Lattice Experiment

Volker Schilling

Masterarbeit in Physik
angefertigt im Institut für Angewandte Physik

vorgelegt der
Mathematisch-Naturwissenschaftlichen Fakultät
der
Rheinischen Friedrich-Wilhelms-Universität
Bonn

November 2015

1. Gutachter: Prof. Dr. Dieter Meschede
2. Gutachterin: Priv.-Doz. Dr. Elisabeth Soergel

Abstract

This master thesis contains two major parts. On the theoretical side simulating the state-dependent transport of neutral caesium atoms in a two-dimensional optical lattice gives an intuitive picture of the state-dependent potential during transport. The more practical part deals with the task to load the atoms into the lattice since they cannot be trapped directly in the plane of the experiment. A magneto-optical trap in a distance of about ~ 2 mm below the lattice traps atoms out of the vacuum background and lift them afterwards into the lattice. This is realised using a precise electronic control of the imbalance of current guided through the two coils for building up the required quadrupole field by diverting a certain amount of current around one coil. Analysis of the step-response signal of the used metal band coils yields mandatory characteristics for achieving a fast and stable control. A galvanic isolated signal transfer protects the computer control against damage due to accidental voltage pulses from the high-power system. The diverted current can change with $\sim 0.9 \text{ A ms}^{-1}$.

Contents

1	Introduction	1
2	Cooling and trapping atoms	3
2.1	Magneto-optical trap	3
2.2	Dipole traps	3
2.2.1	State dependent dipole traps and system specific wavelength	4
2.2.2	State dependent transport	5
2.2.3	Two-dimensional state dependent optical lattice	5
2.3	Experimental Setup	6
2.3.1	Vacuum system	6
2.3.2	Imaging system	7
2.3.3	Laser cooling system	7
3	Simulation of two dimensional transport	9
3.1	General Explanation	9
3.1.1	Simulation of state dependent transport	10
3.1.2	Potential depth during transport	11
3.2	Outlook	12
4	Magnetic elevator for trapped ^{133}Cs atoms	15
4.1	Required magnetic fields	15
4.2	Implementation of magnetic field gradients	16
4.3	Characterisation of the anti Helmholtz coils	17
4.4	Realisation of current driver for elevating atoms	19
4.4.1	Control of asymmetrically coil currents	19
4.4.2	Passive stabilization with snubber circuit	20
4.4.3	Galvanic isolated signal transfer	21
4.5	Thermal analysis	24
4.5.1	Thermal properties	24
4.5.2	Heat dissipation	26
4.6	Outlook	27
5	Summary	29
	Bibliography	31
A	Additional explanations / data	33
A.1	Inductivity using LR -circuit	33
A.2	Inductivity using LC -circuit	34

A.3 Capacity using <i>LC</i> -circuit	35
List of Figures	37
List of Tables	39
Acronyms	41

Introduction

Understanding of processes in nature can be verified by simulating the observed effects. An exact analysis of the process in a finite number of logical operations is possible if the simulator is doing exactly the same as nature does [1]. Certain quantum mechanical systems have already been investigated using different environments, for instance ions in Paul traps to investigate entanglement [2], neutral atoms in a two-dimensional optical lattice investigating Mott-insulators [3] or photons in fibre networks to perform two-dimensional quantum walks [4].

A quantum walk is the quantum analog of the classical random walk. While the walker's position is classically described by a Gaussian probability distribution, where the covered mean square distance σ^2 of the walker increases linear with time ($\sigma^2 \propto t$), forming a Bell-shaped curve, quantum mechanical superposition results in a quadratic increase over time ($\sigma^2 \propto t^2$) [5]. Applied to certain tasks, for instance looking for a special entry in an unordered database, a random walk based algorithm would choose an entry randomly after the other while quantum walk based algorithms exploit interference of every entry's result simultaneously, ending up at the final entry quadratically faster than its classical counterpart. This can be seen as a faster information spreading. While in continuous-time quantum walks an unitary operation, applied to a Hamiltonian fully describes its time evolution, discrete-time quantum walks consist of two operations. The "coin" operation is acting on the state and the "shift" operation acts on the walker's position. As an example of a discrete time quantum walk on a line, the coin space is two-dimensional and can be represented by any two-level system.

In the quantum technologies group in Bonn we work on the realization of discrete-time quantum walks of neutral atoms in state-dependent optical lattices. In our experiments, we use single caesium atoms as a quantum walker providing the two-level system defining its qubit states $|\uparrow\rangle$ and $|\downarrow\rangle$ to its two outermost hyperfine ground state levels. An external coherent microwave pulse realizes the "coin" operation while changing the atom's state [3]. Operating the state-dependent optical lattice changes the atom's position and realizes the "shift" operation. The state-dependent lattice consists of two similar overlapping standing wave dipole traps, each created by an original scheme based on the dynamical synthesis of light polarization.

In an already established experiment, we realize one-dimensional discrete-time quantum walks with neutral atoms to investigate for instance Bloch oscillations in a simulated electric field [6]. Additionally to this, we currently build an apparatus to perform quantum walk experiments with neutral atoms in two-dimensions. This will enable us to investigate two-dimensional problems for instance the dispersion relation of electrons in graphene. The lattice is placed in an in-house built dodecagonal vacuum glass-cell [7]. Its ultra-low birefringence supports precise polarisation synthesis of the laser beams without disturbances. The solid immersion of our in-vacuum, high numerical aperture (NA = 0.92) objective will

enable single site resolution of single atoms in an optical lattice with a lattice constant of 612 nm. In this thesis I will explain how the two dimensional state dependent transport happens. To achieve this I will start in chapter two with basic information about the used cooling and trapping mechanisms. Afterwards I explain in chapter three how I simulated the transport procedure within the two-dimensional lattice using Mathematica and in chapter four how the necessary magnetic elevator for the atoms is driven by a current diverter board which I designed and included in the experimental setup during the last year. Chapter five will summarize the necessary steps to have a working elevator for atoms in place now.

Cooling and trapping atoms

The [discrete quantum simulation \(DQSIM\)](#) experiment is designed to investigate physics in a [two-dimensional state-dependent optical lattice \(2D-SDL\)](#). Our primary interest focussed on studying small ensembles of atoms, which allow us to form a small [magneto-optical trap \(MOT\)](#) directly in the science chamber. This [MOT](#) serves as a source of cold atoms, however, due to the high-[numerical aperture \(NA\)](#) objective (see section [2.3.2](#)) we are unable to load the atoms directly from the [MOT](#) into the optical lattice. Instead we employ a so called magnetic elevator to move the atoms. Since we are primarily interested in small ensembles of atoms, we can start the experiment by simply loading a [MOT](#) directly inside the science chamber. Once the atoms are in the [2D-SDL](#) we use an additional lattice along the z -axis to achieve a strong confinement in all three dimension. In this position we can illuminate them using molasses laser beams, which allow us to take fluorescence images with single site resolution using our high-[NA](#) objective. The lifetime of the trapped atoms is limited by collisions with the thermal background gas. In our experimental apparatus, the science chamber consists of an [ultra-high vacuum \(UHV\)](#) glass cell with ultra low birefringence [\[7\]](#).

2.1 Magneto-optical trap

Dilute caesium atoms in the vacuum chamber are in thermal equilibrium with the surrounding at room temperature. In contrast the potential in the state dependent optical lattice is below 1 mK and therefore the atoms need to be cooled. To capture caesium atoms out the background vapour and cool them to the Doppler temperature we use a [MOT](#). The basic principle of a [MOT](#) is velocity dependent Doppler cooling combined with a position dependent force. The position dependency results on circular polarised dipole transitions in a magnetic quadrupole field (see figure [2.1](#)). The atoms are trapped in the centre of a magnetic quadrupole field generated by a pair of anti Helmholtz coils at the point of $\vec{B} = 0$. The cloud of cooled atoms can therefore be shifted in space by changing the zero point of this magnetic quadrupole field, i.e. by applying an additional homogeneous magnetic offset field using coils in Helmholtz configuration. An in depth description of a [MOT](#) in general and of the [MOT](#) used in a similar experiment can be found in [\[8–10\]](#).

2.2 Dipole traps

An optical dipole trap exploits the potential created by an alternating electrical light field several nm detuned from a resonance of a dipole transition. Following the calculation (shown in [\[12\]](#)) of an induced

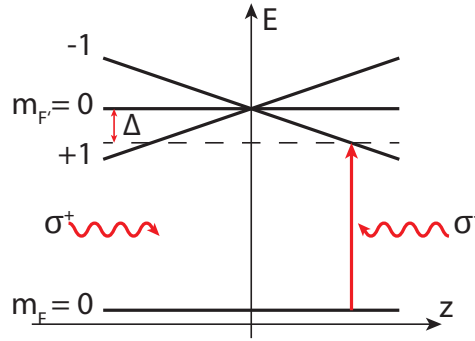


Figure 2.1: Principle of a one-dimensional MOT: Magnetic gradient field along z -direction, with $\vec{B} = 0$ at $z = 0$. The energy splitting of the m_F levels is proportional to \vec{B} . Red detuned σ^\pm polarized light is resonant in dependency on the atoms velocity and position. (adapted from [11])

dipole moment \vec{p} with an electrical field \vec{E} yields the dipole potential

$$U_{\text{dip}}(\omega) = \frac{3\pi c^2}{2\omega_0^3} \frac{\gamma}{(\omega - \omega_0)} I \quad (2.1)$$

with the vacuum speed of light c , the natural linewidth γ and the resonance frequency of the dipole transition ω_0 which is proportional to the light intensity I and depending on the trapping laser frequency ω . In case of a trapping frequency ω smaller than the resonance frequency ω_0 equation 2.1 becomes negative, which leads to an attractive potential in high intensity regions. In contrary, for trap frequencies bigger than ω_0 the potential becomes the opposite sign, meaning that atoms get repelled from high intensity regions and can instead be trapped in the minimum, which is referred to as a blue detuned optical dipole trap. To realize a state dependent trap one can exploit both effects, as discussed in the following section.

2.2.1 State dependent dipole traps and system specific wavelength

We define the atomic qubit state using the two outermost hyperfine ground state levels $|\uparrow\rangle = |F = 4, m_F = 4\rangle$ and $|\downarrow\rangle = |F = 3, m_F = 3\rangle$ of caesium. Figure 2.2(a) shows a simplified level scheme with neglected hyperfine structure. By applying a **direct current (DC)** magnetic field as quantisation axis parallel to the trapping laser beams, a circular polarized optical standing wave pattern induces σ^+ or σ^- dependent optical dipole traps. The σ^- lattice for the $|\uparrow\rangle$ state is red detuned to the $^2P_{3/2}$ level (referred to as D_1 transition) and blue detuned to the $^2P_{3/2}$ level (referred to as D_2 transition). Due to the non existing $m_J = \frac{3}{2}(-\frac{3}{2})$ states of the $^2P_{1/2}$ level an atom in $|\uparrow\rangle$ ($|\downarrow\rangle$) state will experience an attractive potential from the σ^+ (σ^-) polarised light, while for σ^- (σ^+) polarised light it experience both an attractive potential for the D_2 transition and a repulsive potential for the D_1 transition. Choosing the **system specific wavelength** (λ_m) the effective potential for these two contributions cancel out and the remaining σ^+ (σ^-) lattice consists only of red detuned contribution of the D_2 transition. For detailed calculation and explanation see the theses [10, 11, 14]. In our experiment we exploit this state dependency to form a spin dependent optical lattice by creating two independent optical lattices. These lattices are generated by two superimposed laser beams with optical circular polarisation that interfere with a third counter propagating laser beam with linear polarisation (see figure 2.2(b)).

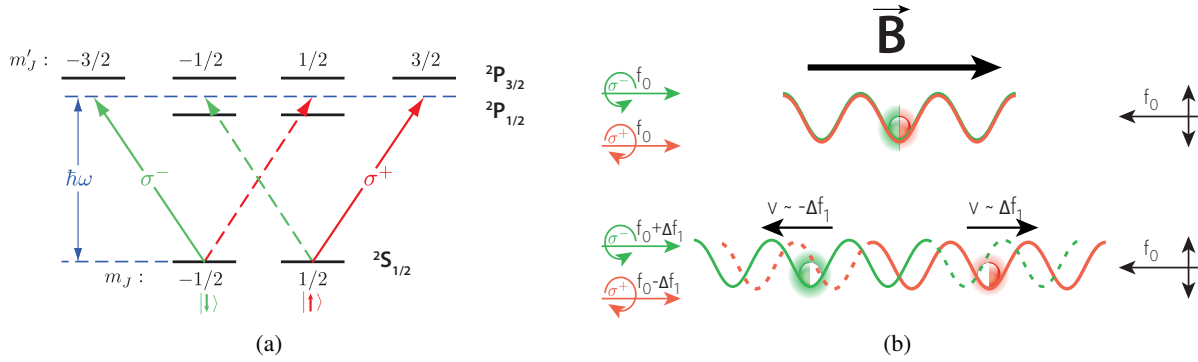


Figure 2.2: State dependent transport: (a) Level scheme of ^{133}Cs without hyperfine structure. The D_1 transition connects the $2S_{1/2}$ -level to the $2P_{1/2}$ -level while the D_2 transition connects the $2S_{1/2}$ and the $2P_{3/2}$ -level. The frequency ω is related to the system specific wavelength λ_m [11]. (b) One laser beam, consisting of precise synthesized σ^+ and σ^- polarized light, propagates parallel to a magnetic field. Together with the counter propagating linear polarized laser beam it creates a standing wave dipole trap. Variation in the circular polarized frequency leads to moving lattice potentials. [13]

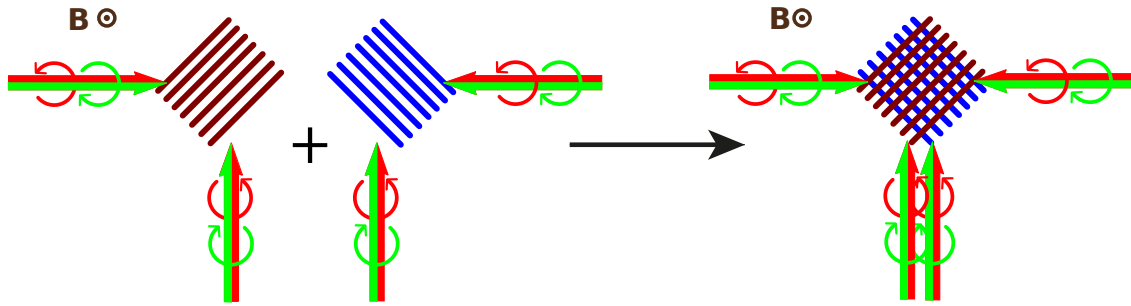


Figure 2.3: The two-dimensional lattice is constructed by two one-dimensional lattices. The different colours show the frequency difference of 160 MHz. The electric field of every laser beam is orthogonal to the magnetic field.

2.2.2 State dependent transport

The state dependent transport as explained in the previous section has been realised in one dimension in another experiment [10]. To control the atom's positions slightly shifting the phase with respect to each other shifts the lattice sites. In the laboratory, an **acousto-optic modulator (AOM)** constructs a tiny frequency difference of the corresponding laser beams resulting into a changing phase relation and therefore into lattice velocity proportional to the frequency difference. Superposition of σ^+ and σ^- polarised laser beams yields an effective linear polarisation. Since it is sufficient to change the frequency on one side the constant phase relation will further on be marked as a linear polarised laser beam.

2.2.3 Two-dimensional state dependent optical lattice

In the **DQSIM** experiment we want to extend this to two dimensions, however, simply installing an additional orthogonal state dependent lattice would not work since the quantisation axis introduces π contributions to one dimension. Precise frequency synthesis of every laser beam and turning the quantisation axis orthogonal to every lattice laser beam provide an working lattice scheme to perform two dimensional state dependent transport. With respect to the hyperfine structure the resulting trap

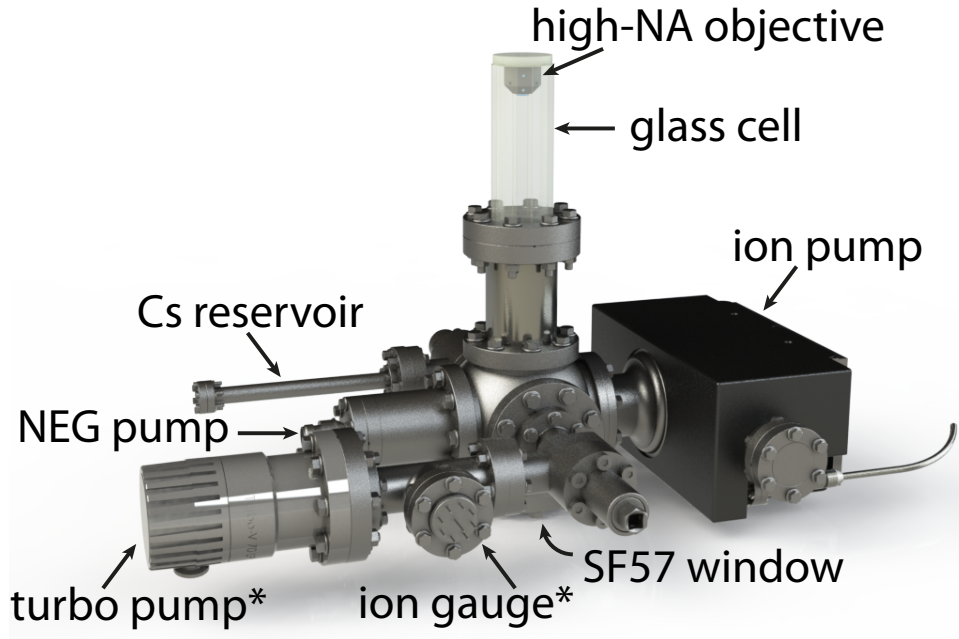


Figure 2.4: Vacuum system: Functional parts are labelled. The *-symbol marks parts which helped to establish the vacuum and are removed now [16].

potentials would be

$$\begin{aligned}
 U_{|\uparrow\rangle} &= U_{\sigma^+} + U_{\pi} \\
 U_{|\downarrow\rangle} &= \frac{7}{8}U_{\sigma^+} + \frac{1}{8}U_{\sigma^+} + U_{\pi}
 \end{aligned}
 \tag{2.2}$$

Intersecting the corresponding laser beams within an angle of 90° yields an 45° rotated standing wave dipole lattice with an enlarged lattice constant of $d = \lambda_m / \sqrt{2}$, that can be single site resolved by our high-NA objective. The working principle of this configuration and an analysis of its transport and potential behaviour is explained in detail in chapter 3.

2.3 Experimental Setup

In the following I will introduce the main components of the experimental apparatus, which includes the vacuum maintenance apparatuses and the optical and mechanical details to run the experiment.

2.3.1 Vacuum system

The vacuum system contains the in-house designed and constructed high-NA objective [15] which is glued in an in-house built glass cell as well as the vacuum maintenance machines. The experiments take place inside the glass cell [7] in a distance of about $150 \mu\text{m}$ below the objective. The entire experiment chamber is sketched in figure 2.4.

Vacuum system The vacuum chamber is designed such that it can be mounted below an optical bread board with a whole, such that no component hinders the optical paths which are all going into the glass cell. An ion pump in combination with a [non-evaporable getter pump \(NEG-pump\)](#) binds residual gas molecules and atoms. Heating the caesium reservoir supports the vacuum pressure below 1×10^{-10} mbar as well as providing a background caesium vapour. A vacuum tube connects this area to the twelve-sided glass cell where the experiments take place.

Ultra-high-vacuum glass cell The in-house built cylindrical twelve-sided glass cell is made of SF57 and the ultra-low birefringence of $\sim 1 \times 10^{-7}$ [7] allows for precise polarisation control which is crucial to establish and control the state-dependent optical lattice. The in-house designed vacuum compatible objective is glued at the ceiling and is the central part of the imaging system.

2.3.2 Imaging system

High-numerical aperture objective The central part of the imaging system is the in vacuum objective providing a high-NA of 0.92 yields an imaging resolution of 565 nm. It is designed for imaging caesium atoms in single lattice sites of 612 nm distance, emitting light on the D₂ transition at $\lambda_{D_2} = 852$ nm and provides diffraction limited imaging in a field of view with a width of 70 μm which is related to 120 lattice sites [17]. The images are acquired by an [electron multiplying charge-coupled device \(EMCCD\)](#) camera (Andor iXon3).

2.3.3 Laser cooling system

Magneto-optical trap The [MOT](#) is created by laser beams which are red detuned to the D₂ transition at 852 nm [18] and pumps the almost closed transition from $F = 4$ to $F' = 5$. The Doppler temperature for this transition is $T_D = 126 \mu\text{K}$. A re-pumping laser pumping the transition from $F = 3$ level to $F' = 4$ brings the off resonant excited atoms back to the cooling cycle. The cooled atoms are left in the $|\uparrow\rangle$ state [10]. The cooling laser beam diameters of $d_{\text{cool}} = 2.2$ mm and a magnetic field gradient of ~ 80 G/cm establishes the [MOT](#). Because of the objective's working distance of 150 μm the cooling beams would be clipped at the objective's edge and therefore the [MOT](#) is loaded 2 mm below with a subsequent transport of the atoms upwards.

Magnetic elevator To load the [MOT](#) 2 mm below, the magnetic quadrupole field needs to be shifted down. To transport the trapped atoms upwards to the [2D-SDL](#) they just follow the point of $\vec{B} = 0$. This starts shifting the [MOT](#) and is combined with the principle of magnetic transport [19] when leaving the area of present [MOT](#) laser beams. Both of these two principles are based on shifting the magnetic quadrupole field. The construction of this magnetic elevator is explained in more detail in chapter 4.

Horizontal confinement The [2D-SDL](#) consists of two independently controllable one dimensional lattices. Both operating at the system specific wavelength (see chapter 2.2.1) of $\lambda_m = 866$ nm [11] detuned with respect to each other by 160 MHz to prevent interference. To achieve nearly homogeneous horizontal intensity while preventing stray light resulting from the laser beams clipping at the objective's edge, the beam profile at the position of the trap is elliptically with a horizontal beam waist of 52 μm and a vertical beam waist of 145 μm .

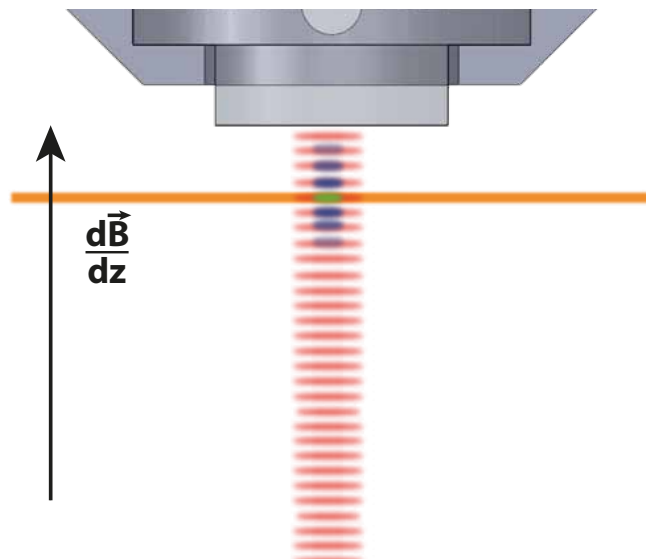


Figure 2.5: The z -dipole trap beam is back reflected at the objective's surface and establishes a standing wave dipole trap. The blue spots symbolise the atom cloud divided into several lattice sites. The green spot is the remaining lattice site after selection in a magnetic gradient field and removing of atoms in the other lattice sites [20] and is subsequently operated by the (orange) two dimensional state dependent optical lattice.

Vertical confinement A laser beam with a wavelength of $\lambda_z = 1\,064\text{ nm}$, pointing vertically upwards is back reflected at the objective's surface creating a standing wave dipole trap. Since we want to work within the focus depth of $1\ \mu\text{m}$ of our objective and image only a single plane of the z -axis, but loading the MOT in the lattice will populate multiple places we require a mechanism to select a single one by applying a magnetic gradient field along the z -axis [20]. A resonant microwave field changes the qubit state in the desired lattice site from $|\uparrow\rangle$ to $|\downarrow\rangle$ [21] and a following push out laser beam resonant to the $|\uparrow\rangle$ state removes these atoms from the other lattice sites. Figure 2.5 shows this process including the orange horizontal two dimensional lattice beams. The z -dipole trap stays switched on during the experiment and provide vertical confinement.

Simulation of two dimensional transport

The previous part of this thesis described the general setup and mechanisms we are going to use in the experiment. The general description of the working principle is used in a simulation of the state dependent transport in Mathematica with simplification to one dimension. Detailed analysis of the potential contributions of the different polarisations resulting from the decomposed laser light field gives information how to perform state dependent transport with respect to the potential depth during transport.

3.1 General Explanation

As mentioned before, the atoms are constrained in the xy -direction by the **2D-SDL** and in the z -direction by a state independent standing wave dipole trap. Thus, atoms are stored in a three dimensional potential where two dimensions are state-dependent. The vertical dipole trap is required to keep the atoms in the $1\ \mu\text{m}$ wide depth of focus [15] of our objective.

An effective two dimensional system is realised by selecting a single slice of atoms. The atoms are trapped in a standing wave dipole trap consisting of linear polarized light back reflected at the objective's surface. The Potential depth at the **2D-SDL** $150\ \mu\text{m}$ below is calculated for a Gaussian distributed laser beam profile with a beam waist of $w_{0z} = 75\ \mu\text{m}$ at the surface of our objective and a laser power of $5\ \text{W}$ at a wavelength of $\lambda_z = 1\ 064\ \text{nm}$. Following [11, 12, 22] this yields a trap depth of $U_{z\text{-dip}} = 587.4\ \mu\text{K}$ for $|\uparrow\rangle$ state in the retro reflected configuration. Along the horizontal directions (x, y) state dependent transport is available. The decomposed polarisations of the horizontal **2D-SDL** laser beams contribute to the horizontal dipole potential when the resulting linear polarisation contains an electrical field orthogonal to the quantisation axis. Calculating the dipole potential of the lattice laser beams envelope function leads to a normalised horizontal dipole potential. Figure 3.1(a) shows the one dimensional potential for the $|\uparrow\rangle$ -state in red and the $|\downarrow\rangle$ -state in green in case of only slightly shifted lattice potential near the **maximal potential depth** (U_{max}). Figure 3.1(b) shows an example of the case of a small horizontal lattice potential due to shifted potential wells of the state dependent contribution and the state independent π -contribution to the potential. In this case, the horizontal lattice potential is below zero and traps atoms in the **intensity maximum** (I_{max}) but different horizontal lattice sites can hardly be distinguished. The potential depth, which is mentioned here defines the potential between two neighbouring lattice sites for a certain qubit (qualitative analysis below). The effective horizontal lattice potential is the potential between two lattice sites (marked by orange lines in figure 3.1).

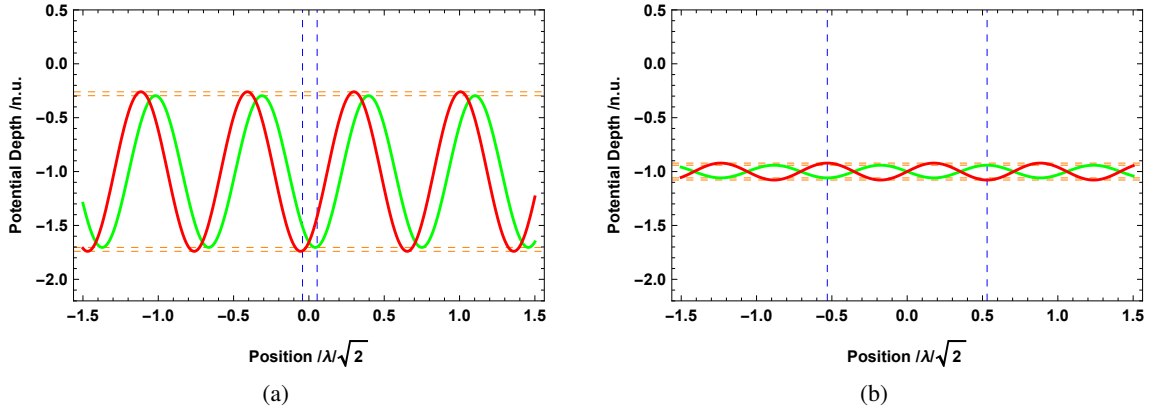


Figure 3.1: Two-dimensional potential in normalised units (n.u.) for the $|\uparrow\rangle$ -state (red) and the $|\downarrow\rangle$ -state (green) for two different settings of the polarisation angles Θ_1 and Θ_2 as defined in figure 3.2(a). **(a)**: $\Theta_1 = 0.2\pi$, $\Theta_2 = 0.2\pi$: The two dimensional potential is deep and atoms can be trapped in certain lattice sites. **(b)**: $\Theta_1 = 0.025\pi$, $\Theta_2 = 0.5\pi$: The shallow two dimensional potential is in general below zero and traps atoms in the beam's intensity maximum. Trapping atoms in certain lattice sites and subsequently state dependent transport is hardly possible.

3.1.1 Simulation of state dependent transport

The following section elucidates a simulation of state dependent transport using Mathematica [23], performed with two linear polarised laser beams, intersecting each other by an angle of 90° providing a single side resolved lattice distance of $d_{2D} = \frac{866}{\sqrt{2}}\text{nm}$.

Configuration The simulation starts describing the electric fields of the involved laser beams as a plane wave in the xy -plane as

$$\vec{E}_{\text{lin}} = E_0 \cdot \hat{e}_{\text{lin}} \cdot e^{i\vec{k}\vec{x} - i\omega_1 t} \quad (3.1)$$

with the wave vector $\vec{k} = \frac{2\pi}{\lambda} \begin{pmatrix} \cos(\phi) \\ \sin(\phi) \\ 0 \end{pmatrix}$ directed into the direction of the propagating laser beam with an

unity electric field E_0 , the laser frequency $\omega_1 = 2\pi \frac{c}{\lambda_1}$ and a linear polarisation vector $\hat{e}_{\text{lin}} = \begin{pmatrix} 0 \\ \sin(\Theta) \\ \cos(\Theta) \end{pmatrix}$.

Treatment of a planar wave holds since the calculated area is small in the middle of the horizontal Rayleigh length of $z_R = 21.5\text{mm}$. The phase shift between the circular polarised laser beams results in an equivalent linear polarisation described by the angle Θ . Rotation for $\pm 45^\circ$ around z -axis rotates the two laser beams in opposite directions and let them intersect each other in the origin. The transformation into the circular basis is realised by multiplication with matrix M defined as

$$M \cdot \vec{x} = \begin{pmatrix} \frac{1}{\sqrt{2}} & \frac{i}{\sqrt{2}} & 0 \\ \frac{1}{\sqrt{2}} & \frac{-i}{\sqrt{2}} & 0 \\ 0 & 0 & 1 \end{pmatrix} \cdot \begin{pmatrix} x \\ y \\ z \end{pmatrix} = \begin{pmatrix} \sigma^+ \\ \sigma^- \\ \pi \end{pmatrix}. \quad (3.2)$$

Connecting the electric field vector in circular basis (\vec{E}_{circ}) to the intensity $I_l \propto |\vec{E}_{\text{circ}}|^2$ enable a qualitative simulation of the one-dimensional state-dependent optical lattice (1D-SDL) where the separate

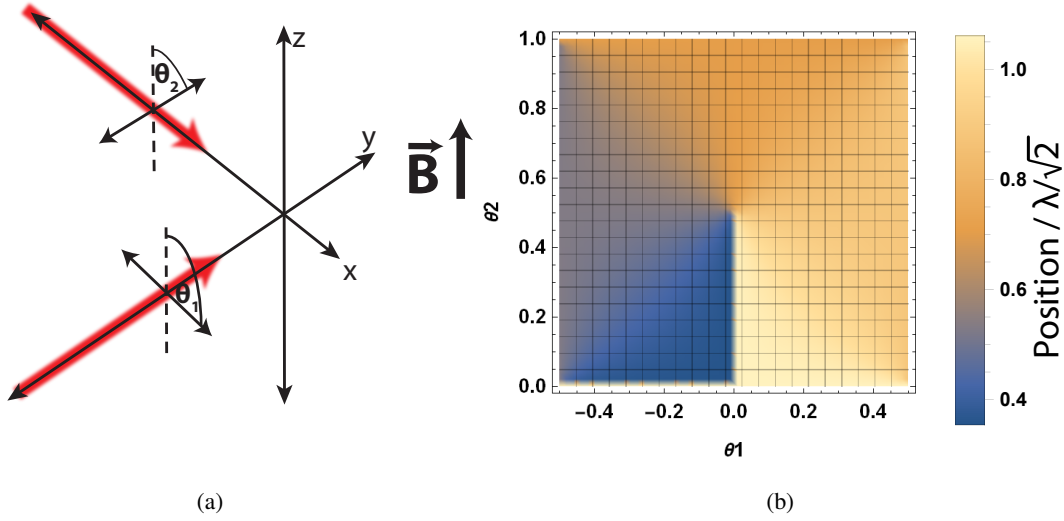


Figure 3.2: **(a)**: Configuration for simulation of **1D-SDL**: Two orthogonal polarisation synthesized laser beams intersecting in the origin. The phase shift of the two circular polarisations is expressed as the linear polarisation angle Θ_1 and Θ_2 respectively. **(b)**: Displacement of the $|\uparrow\rangle$ potential well from the origin for different polarisation angles Θ_1 and Θ_2 . The displacement is visualised by different colours on the map. One turn on the map leads to a displacement of one lattice site. The discontinuity at $\Theta_1 = 0$ symbolise the lattice potential to be the same after transporting one qubit for one lattice site.

components for σ^+ , σ^- and π -polarised light are directly connected to the potential components acting on the qubit states (see equation 2.2).

State-dependent transport The position of the $|\uparrow\rangle$ qubit potential related to the origin, demonstrated in figure 3.2(a) is mapped in figure 3.2(b) for possible configurations of Θ_1 and Θ_2 . Different colours symbolise different displacements. The periodicity of $\lambda/2$ limits the complexity to angles from $\Theta_{1,2} = 0$ to π . Transporting the atoms to the next lattice site requires a polarisation synthesized path along a position gradient by means of one circle around the centre point in the map (figure 3.2(b)). After one turn the potential configuration is equal to the start configuration but the atoms are shifted by one lattice site which is symbolised by the discontinuity. A proper transport velocity can be found by modelling a path with a desired displacement gradient over time.

3.1.2 Potential depth during transport

Additionally to the transport velocity, it is important to control the potential depth during transport since an unwanted fluctuating dipole potential can heat the atoms and limit coherence. Figure 3.3 shows a map similar to figure 3.2(b) but here, the colour defines the trap potential for a certain configuration of Θ_1 and Θ_2 . The $|\uparrow\rangle$ qubit potential (figure 3.3(a)) for instance provides a constant potential depth by performing the transport along the polarisation synthesis marked by the black square. The same transport configuration will result in a not constant potential for the $|\downarrow\rangle$ qubit. No configuration can provide transport with a constant potential for both qubit states simultaneously. Hence an appropriate transport configuration including the changing potential for one of the two or both qubit states needs to be tailored for the different classes of experiments.

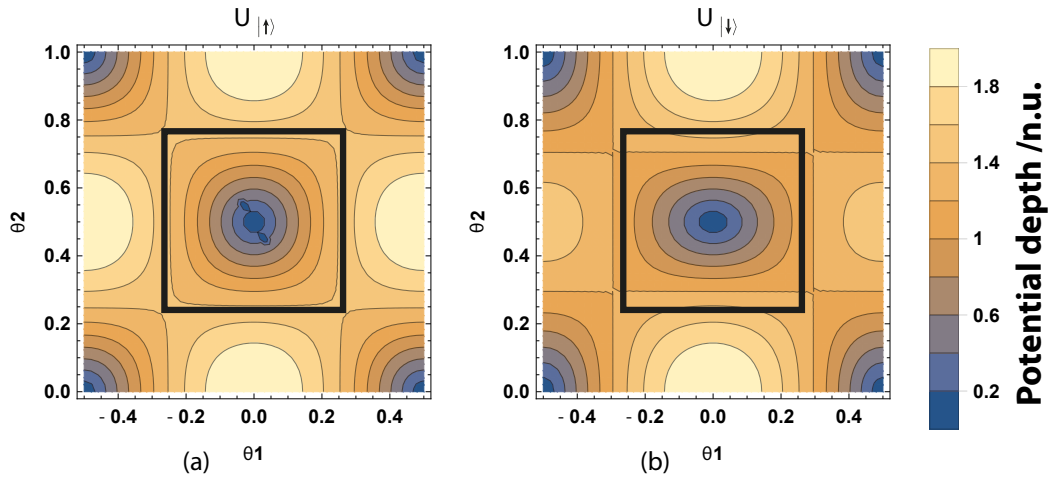


Figure 3.3: Dipole potential depth in a lattice site depending on the polarisation angles Θ_1 and Θ_2 . The potential depth inside the state-dependent lattice is the difference between the maximal and the minimal potential for each configuration (see figure 3.1). The potential depth is displayed using colours. Equal potentials are marked using height lines. **(a)**: Potential mapping for the state $|\uparrow\rangle$. A path with constant potential depth is along a square on the map. **(b)**: Potential mapping for the state $|\downarrow\rangle$. The potential depth, symbolised by the colour is differently distributed compared to the state $|\uparrow\rangle$ and therefore lead to different potentials acting on atoms in the two qubit states during transport.

	Quantisation orthogonal	Quantisation parallel
required synthesized beams	4	2
single site resolution	yes	yes
present π contribution	yes	no

Table 3.1: Comparison between the simulated transport scheme with an quantisation axis orthogonal and the novel transport scheme with the quantisation axis parallel to the 2D-SDL plane.

3.2 Outlook

An improved transport configuration without a containing π -contribution was discussed [16] after I finished my analysis. In this configuration (see figure 3.4), only σ^+ and σ^- polarised light contributes to the state dependent potential since all present electric field vector points orthogonal to the quantisation axis. The absence of π potentials leads to a constant potential depth of the $|\uparrow\rangle$ state. Fortunately the discussed transport scheme can be investigated with just a few modification in my Mathematica-code. Further on it simplifies the installation and operation of the two-dimensional transport a lot since it is easier to adjust and operate, when two lattice beams fewer require polarisation synthesis (see table 3.1). Resulting this, four AOM including careful alignment, control and at least space on the optical table can be saved.

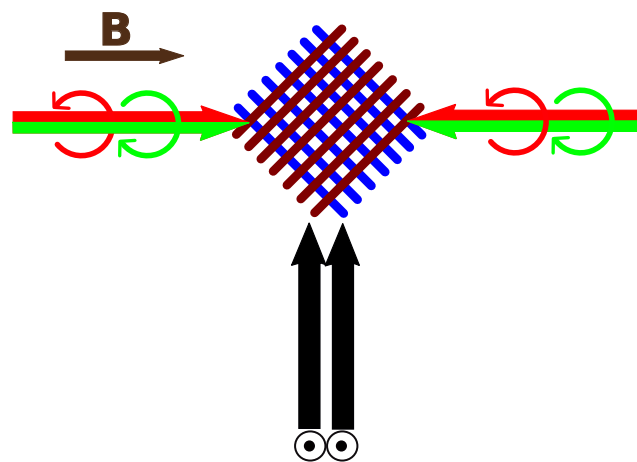


Figure 3.4: Improved state dependent transport schematics: The quantisation axis is parallel to the counter propagating synthesized laser beams. The corresponding linear polarised laser beams contains only electrical field components orthogonal to the quantisation axis.

Magnetic elevator for trapped ^{133}Cs atoms

Experimental verification of these simulation presupposes having a controllable state dependent optical lattice as well as the presence of caesium atoms trapped in it. The standard tool for capturing atoms out of the background vapour of an UHV cell into a MOT cannot be used at the position of the 2D-SDL in a distance of $d_l = 150\ \mu\text{m}$ beneath the high-NA objective. The MOT laser beams with a diameter of about $w_{\text{MOT}} = 2\ \text{mm}$ would be clipped at the edge of the objective producing stray light and random reflections. Subsequently the MOT needs to be established at a point around $d \approx 2\ \text{mm}$ below the 2D-SDL in a magnetic quadrupole field with a gradient of $d\vec{B}/dt \sim 80\ \text{G/cm}$ at the position where the magnetic field is $\vec{B} = 0$. Henceforth compressing the MOT and select a certain slice of atoms to load the 2D-SDL requires a magnetic gradient of up to $d\vec{B}/dt \sim 300\ \text{G/cm}$ directly at the position of the 2D-SDL $150\ \mu\text{m}$ below the high-NA objective. This chapter deals with the problem to provide magnetic quadrupole fields at different times of the experiment cycle with different magnetic field gradients providing $\vec{B} = 0$ at different positions.

4.1 Required magnetic fields

As mentioned above, the selection of a slice of atoms in the objective's focal plane requires a high magnetic field gradient of $d\vec{B}/dt \sim 300\ \text{G/cm}$ with the point of zero magnetic field exactly there. At a current guided through the gradient coils of $I = 32\ \text{A}$, resulting in a magnetic field gradient of $d\vec{B}/dt \sim 303\ \text{G/cm}$ a current imbalance of $\Delta I = 2\ \%$ is enough to select the atoms out of focus which can already happen in case of independent noisy power supplies. In case of a spacial fluctuating magnetic field during the micro wave state manipulation this leads to a not clear defined Rabi oscillation and the selection of Atoms will broaden which makes it impossible to choose just one lattice site. The MOT is more tolerant to the required magnetic gradient field and keeps working even in case the point of $\vec{B} = 0$ is roughly in the middle of the MOT laser beams and using another magnetic field gradient only change the trap volume by a fraction. Therefore the magnetic gradient coils need to be mounted such that $\vec{B} = 0$ is in the objective's focal plane for equal current in both magnetic gradient coils. The magnetic quadrupole field can be shifted to load the atoms in the MOT about $2\ \text{mm}$ below this point. Performing this shift by an homogeneous offset field using the z -compensation coils would be the simplest way but requires too high current since their winding number is smaller than $1/10$ of the gradient coil's winding number (see table 4.1). This chapter describes therefore a control circuit to divert a certain amount of current around the bottom gradient coil to lower the magnetic quadrupole field's position for loading the MOT. Building up this circuit requires a detailed characterisation of the magnetic gradient coils to drive the current as well as a stabilised precise current bypass and finally a galvanic isolated information transfer

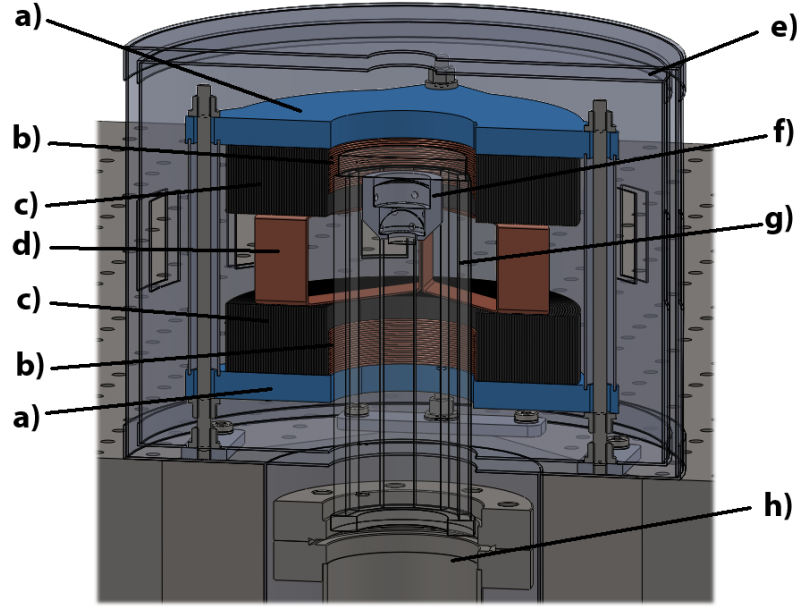


Figure 4.1: Experimental area: **a)** water cooled plates, **b)** z -compensation coils, **c)** z -gradient aluminium band coils, **d)** x/y -compensation coils, **e)** double-layer μ -metal shielding against high frequent magnetic fields, **f)** high NA-objective (NA = 0.92) [17], **g)** twelve-sided vacuum glass cell [7], **h)** connection to vacuum maintaining system (see section 2.3.1).

Coil	gradient	x/y -compensation	z -compensation
material	aluminium band	copper wire	copper wire
conductor area	$(0.15 \text{ mm} \times 30 \text{ mm})$	$\pi \cdot (0.4\text{mm})^2$	$\pi \cdot (0.4\text{mm})^2$
No. of windings	260	20	21
magnetic field per 1 A	33.7 G	1.6 G	3.2 G
magnetic gradient field per 1 A	9.5 G/cm	—	1.4 G/cm

Table 4.1: Dimensions and properties of the different coils used in the experiment. The magnetic (gradient) field is calculated using MatLab [16] and previous characterisation of the coils [16].

to protect the computer control system from high voltage damage in case of failure in the high-power circuit including the gradient coils.

4.2 Implementation of magnetic field gradients

The magnetic gradient field required for the MOT is controlled by two metal band coils made of aluminium with oxidation layer for isolation mounted in an anti Helmholtz configuration (see figure 4.1). Three pairs of additional coils in Helmholtz configuration (figure 4.1(b),(d)) optimised to not limit optical access to the science chamber are used. A double layer barrel consisting of μ -metal shield (figure 4.1(e)) the experimental area against high frequency magnetic fields to establish a well defined magnetic field. The dimensional properties of the implemented magnetic coils can be seen in table 4.1 to get a complete picture while in the following only the gradient coils will be important.

4.3 Characterisation of the anti Helmholtz coils

The properties of the magnetic gradient coils in the low frequency range can be modelled by its physical values of the ohmic DC-gradient coil's resistance (R_L), the gradient coil's inductivity (L_L) and gradient coil's capacity (C_L) in an equivalent circuit (see figure 4.2(a)).

Ohmic resistance

Information about R_L can be extracted by measuring the voltage when a constant current is applied to the coils. The resistances of the top and the bottom gradient coil are $R_L = (0.62 \pm 0.01) \Omega$ and $R_L = (0.61 \pm 0.01) \Omega$ respectively at room temperature. These results are included in the overview table for the coil's properties (table 4.2).

Inductance

The Inductance L_L can be estimated by an ideal flat spiral air-core coil, which neglects the fact of having metal band instead of an infinitesimal wire using the formula [24]

$$L = \frac{r^2 N^2}{20r + 28d} \mu\text{H} \quad (4.1)$$

where N is the number of windings, r the mean radius given in cm and d the depth of the coil, that is the difference of the outer and the inner radius, in cm. This estimation yields an inductance of 8.7 mH with an uncertainty below 5 % for the radial dimensions of the aluminium band coils¹.

Besides this estimation the inductance was measured in two ways exploiting the response to a step function. One to quantify exponential decay and the other to analyse the frequency of an oscillating circuit including each coil separately. A voltage signal generated by a function generator is guided across a high resistor to generate the current step function. The following characterisation used several measurements with different output resistances. Detailed values are given in appendix A.

Exponential decay in LR-circuit: The voltage across one gradient coil (U_L) contains information about the coil's inductance. The system is described by the ordinary differential equation $U = L \cdot \dot{I} = \frac{L}{R} \dot{U}$, which is solved by

$$U_L = U_0 e^{-\frac{R}{L}t}. \quad (4.2)$$

Fitting the curve to the response signal (see figure 4.2(b)) gives a relation for $\frac{R}{L}$ where R can be calculated knowing all the DC resistors giving $L_L = (6.0 \pm 0.8) \text{ mH}$ for the top and $L_L = (6.0 \pm 0.5) \text{ mH}$ for the bottom coil's inductance.

Oscillations in LC-circuit: An C_{ext} of about $(100 \pm 20) \mu\text{F}$ parallel to the coil leads to an oscillating current (see figure 4.2(c)) while high impedances are applied at the frequency generator R_0 as well as at the oscilloscope's input channel R_{in} . As measured below, C_L can be neglected since it is several orders of magnitude smaller than C_{ext} . Fitting a damped sinusoidal oscillation to the measurement data gives the frequency of an oscillating LC-circuit and inserting this together with C_{ext} into the formula for the resonance frequency [25]

$$f = \frac{1}{2\pi \sqrt{LC}} \quad (4.3)$$

of an oscillating circuit gives $L_L = (6.4 \pm 0.2) \text{ mH}$ for the top and $L_L = (6.5 \pm 0.1) \text{ mH}$ for the bottom coil after solving it for L . An average value and using Gaussian error propagation yields the averaged

¹ The uncertainty is below 5 % if $d > 0.2r$ [24].

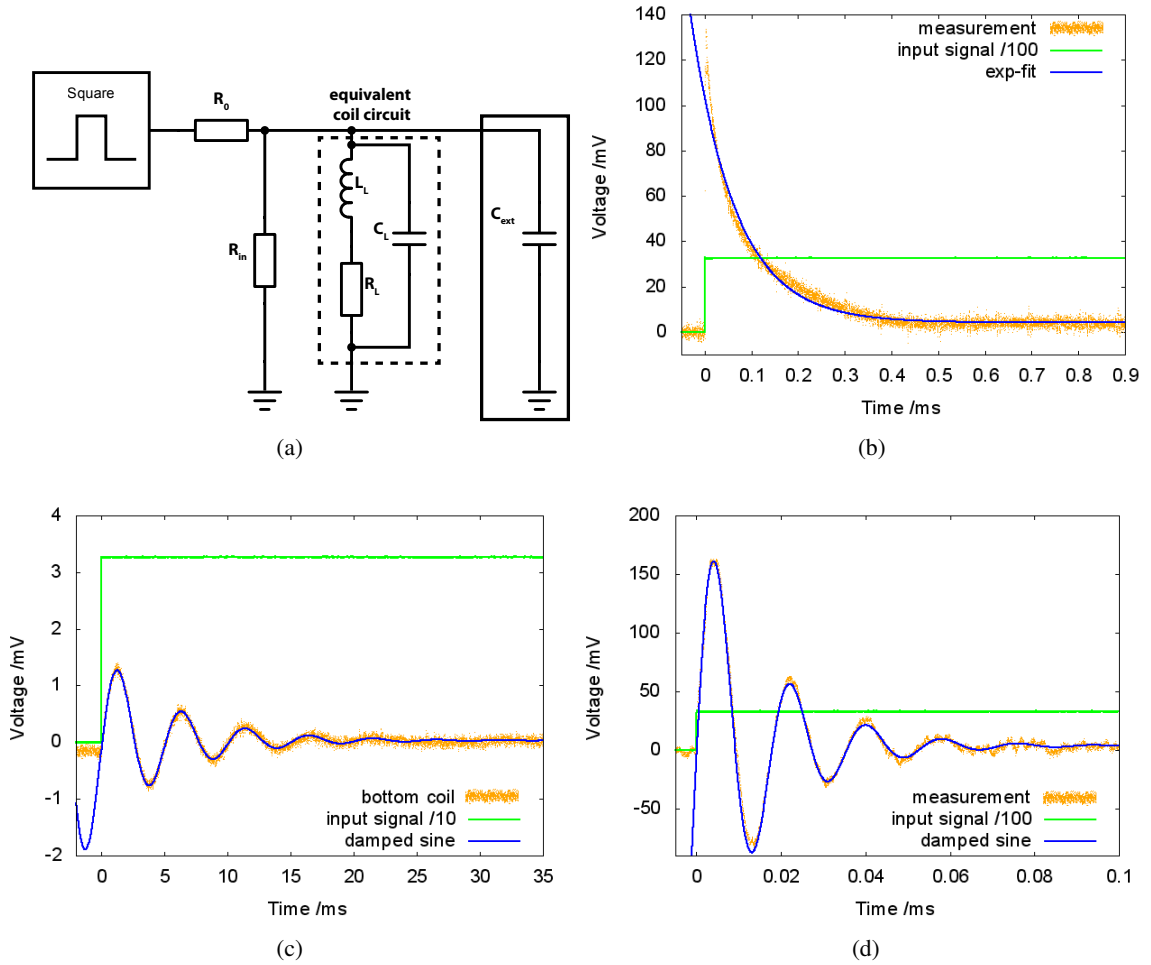


Figure 4.2: Gradient coil's characterisation: **(a)**: Schematic of a coil equivalent measurement circuit for characterisation measurements of the coils. The function generator gives in combination with R_0 a square current signal. An oscilloscope with adjustable input impedance R_{in} measures the voltage across the coil (here: equivalent circuit), and **external capacitance** (C_{ext}) for the measurement of L_L in an LC measurement. **(b)**: Step response in LR -circuit: The exponential decay contains information of L_L (see equation 4.2). **(c)**, **(d)**: Step response in LC -circuit **(c)** with C_{ext} to calculate L_L and **(d)** without C_{ext} to calculate C_L using formula 4.3.

measurement values of $L_L = (6.2 \pm 0.8)$ mH for the top and $L_L = (6.3 \pm 0.5)$ mH for the bottom coil.

Capacitance

Removing C_{ext} enables the LC -circuit to give information about C_L . A highly damped sinusoidal oscillation is fitted to the measured step-response (see figure 4.2(d)). Solving formula 4.3 for C gives a capacity of $C_L = (1.50 \pm 0.20)$ nF for the top and $C_L = (1.31 \pm 0.06)$ nF for the bottom coil with respect to the previous measured inductances.

	top coil	bottom coil
R_L	$(0.62 \pm 0.01) \Omega$	$(0.61 \pm 0.01) \Omega$
L_{calc}	8.7 mH	8.7 mH
L_{meas}	$(6.2 \pm 0.8) \text{ mH}$	$(6.3 \pm 0.5) \text{ mH}$
C	$(1.50 \pm 0.20) \text{ nF}$	$(1.28 \pm 0.07) \text{ nF}$

Table 4.2: The fundamental values required to develop an equivalent circuit which is used for simulation and development of the current bypass circuit. L_{Calc} used equation 4.1. L_{meas} includes $L_{L_{RC}}$ and $L_{L_{LC}}$.

Results

The measured Ohmic resistance of the coils is 3 % below the manufacturers value of $R_L = 0.64 \Omega$ for the top or $R_L = 0.63 \Omega$ respectively for the bottom coil what is slightly out of the error resulting from the measurement. The measured inductivity of $L_L = (6.2 \pm 0.8) \text{ mH}$ for the top and $L_L = (6.3 \pm 0.5) \text{ mH}$ respectively for the bottom coil is about 28 % below the calculated value of $L_L = 8.7 \text{ mH}$ and far out of the given precision [24] for the used approximation. Since the used aluminium band coils are much different to the calculated ideal flat spiral air-core coil the approximation is useful to choose the right order of magnitude. The control circuit for the magnetic gradient coils of another experiment in our group is designed for an inductance $L = 20 \text{ mH}$ and a resistance of $R = 1.6 \Omega$. These coils consists of magnetic coils with each 340 windings of a copper wire with a diameter of 1.4 mm yielding 21.9 G/(cmA) [22].

4.4 Realisation of current driver for elevating atoms

The basic idea of the control circuit is to divert current by a power [metal–oxide–semiconductor field-effect transistor \(MOSFET\)](#) as depicted in figure 4.3. The [MOSFET](#)'s highly non-linear response function is linearised using a feedback [operation amplifier \(OpAmp\)](#) circuit. The amount of bypass current is measured across a [sensing resistance \(\$R_M\$ \)](#) and giving a voltage feedback to the [OpAmp](#) to compare the actual amount of bypass current with the value, given at the input by the computer control.

4.4.1 Control of asymmetrically coil currents

An N-channel power-[MOSFET](#) (IXTH 88N30P) is used to divert the current by changing its resistance. A feedback of measuring the voltage across a sensing resistor $R_M = 0.1 \Omega$ [26] linearises this [MOSFET](#) to enable the driving circuit to control the bypass current precisely. The large gate capacity of more than 6 nF [27] coming from the power-[MOSFET](#)'s large junction area to enable conductivity of large currents and require high driving currents to change the gate voltage fast. The chosen operation amplifier supports up to 150 mA output current but requires special care to avoid hardly controllable oscillations due to its high operation bandwidth of 270 MHz [28]. An operation amplifier supporting a lower bandwidth would require an additional current buffer to drive the [MOSFET](#) properly.

Tuning the feedback loop The integrator circuit (solid square figure 4.4) shifts the operation bandwidth to a lower region. The calculated -3 dB cutoff frequency is defined by a low pass [29] to

$$f_c = \frac{1}{2\pi RC} = 2.8 \text{ MHz.} \quad (4.4)$$

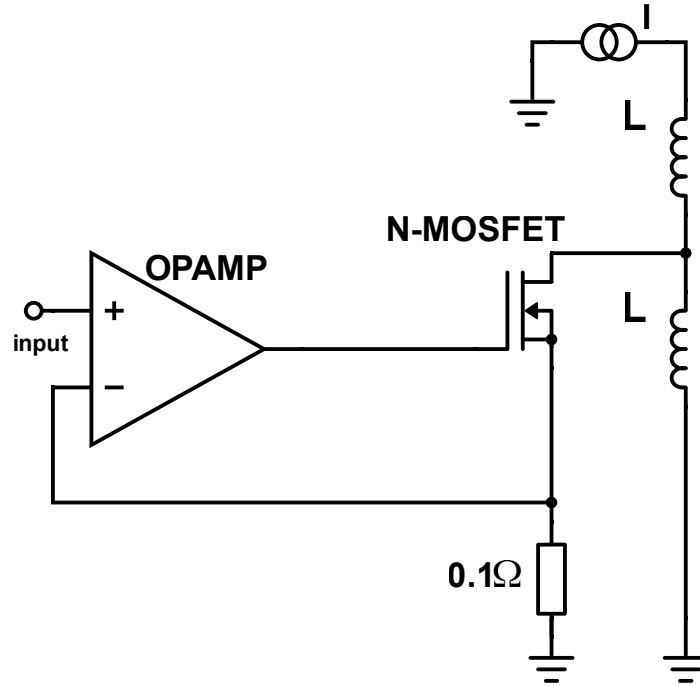


Figure 4.3: Basic idea of current diversion: The power supply gives a constant current through the top and the bottom magnetic gradient coil. A power MOSFET diverts a certain amount of current around the bottom magnetic gradient coil. The voltage of the diverted current measured across a resistor gives feedback to an operation amplifier which compares the feedback voltage with the input signal coming from the computer control and drives the MOSFET.

4.4.2 Passive stabilization with snubber circuit

The equivalent circuit of the magnetic gradient coil acts like a LC oscillation circuit for fast current changes which might occur by running an experimental sequence. This oscillation behaviour is changed by a snubber circuit consisting of a resistance and a capacitance in series to the coil. An aperiodic damping to establish a steady state within a few 10 ms after changing the bypass current can be achieved considering the voltage in the coil equivalent circuits (see figure 4.2(a)). Starting with the formula

$$U_L(t) + U_R(t) + U_C(t) = 0, \quad (4.5)$$

describing the total voltage in this circuit, we use $U_L = L \frac{d}{dt} I$, $U_R = RI$ and $U_C = \frac{Q}{C}$ [30] to get

$$L \frac{d}{dt} I(t) + RI(t) + \frac{Q(t)}{C} = 0. \quad (4.6)$$

Taking the temporal derivative and the Ansatz $I(t) = I_0 \cdot e^{\omega t}$ dividing by L gives the differential equation

$$\omega^2 + \frac{R}{L}\omega + \frac{1}{CL} = 0 \quad (4.7)$$

and using the well known pq -formula to solve this differential equation yields the solutions

$$\omega_{1,2} = -\frac{R}{2L} \pm \sqrt{\frac{R^2}{4L^2} - \frac{1}{CL}}. \quad (4.8)$$

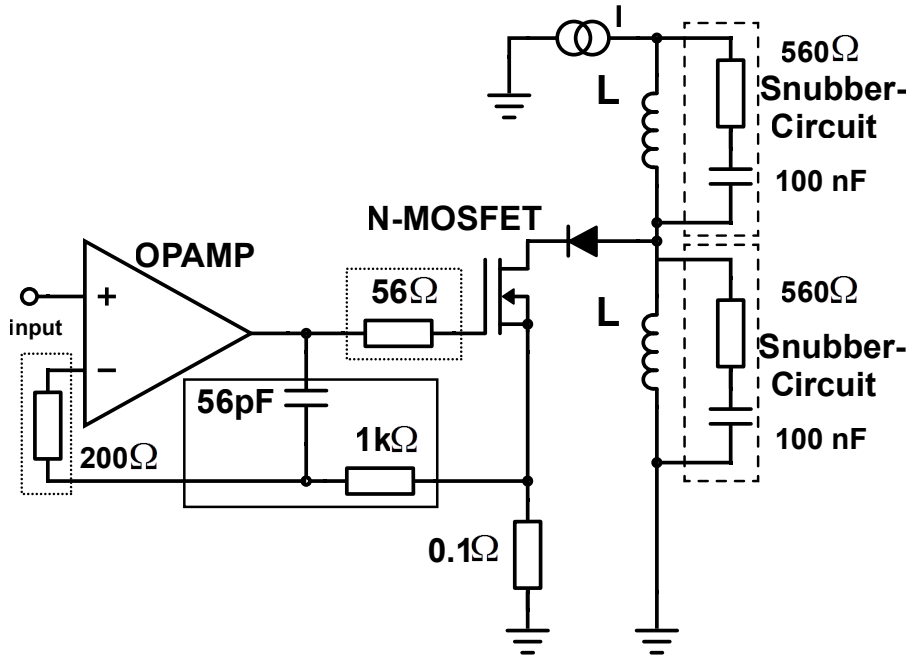


Figure 4.4: MOSFET driving circuit including the two MOT coils L with their snubber circuits (dashed square). The amount of diverted current is measured across $R_M = 0.1 \Omega$. The integrating feedback circuit (solid square) reduces the operating bandwidth to 2.8 MHz. Resistances (dotted boxes) enclose the operating amplifier from capacities.

Aperiodic damping requires the square root to be zero. An external capacitance of $C_S = 100 \text{ nF}$ defines the oscillating frequency (equation 4.3) to $f_L = 6.4 \text{ kHz}$ and leads to the aperiodic damping in case of

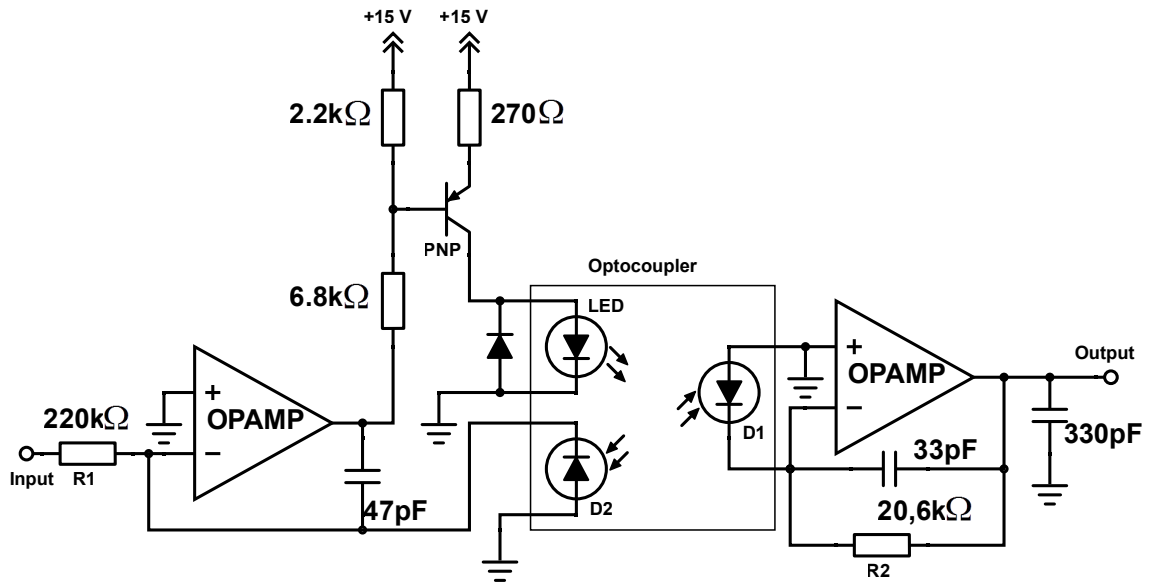
$$R_S = \sqrt{\frac{4L}{C}} = 498 \Omega. \quad (4.9)$$

For practical reasons and to have a magnitude to establish rather slow relaxation, the chosen resistance of 560Ω is a bit bigger than required.

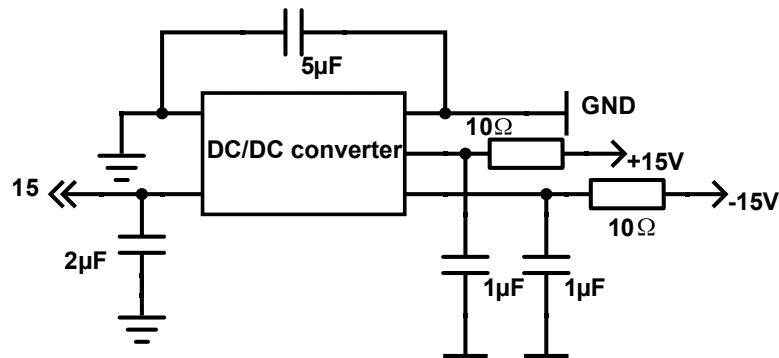
4.4.3 Galvanic isolated signal transfer

The remaining part to complete the current driver circuit is the galvanic isolated signal transfer, realised using an optocoupler and a isolated DC/DC power supply. The basic circuit is adapted from the optocoupler's datasheet [31].

Optocoupler-circuit Figure 4.5(a) shows the used circuit (adapted from [31]) and can be understood as follows: The light emitting diode (LED) driver transforms the voltage signal from the computer control system into a proper current for the LED. The feedback of diode 2 (D2) ensures reliable signal transfer independent from temperature or aging processes. The trans-impedance OpAmp after diode 1 (D1) converts the photo current back into a stabilized voltage signal to drive the current diversion using the previous explained circuit. Tuning resistor R2 with respect to resistor R1 further allow for defining the transfer ratio of the signal. Calibration of the control voltage to the bypass current is essentially based on this ratio and the sensing resistor $R_M = 0.1 \Omega$. Although the ration can be calculated a calibration of this



(a)



(b)

Figure 4.5: (a): Isolated signal transfer: The optocoupler transmits the information from a LED to two photo diodes. The current of D2 builds a feedback signal to stabilise the input signal. The right operation amplifier converts the current of D1 to a voltage at the output (adapted from [31]). (b): The DC/DC converter establish the power supply at the ground free part that is connected to the gradient coil system. $2\mu\text{F}$ at the input side and a 16 kHz low pass filter at the $\pm 15\text{V}$ connection flatten the voltage spikes from the switching power supply.

transfer ratio is required to compensate the tolerances of the used components.

Calibration Enable the computer system to give appropriate commands during a measurement cycle requires a calibration. Figure 4.6(a) shows measured data of the diverted current with respect to the input signal. Positive input signals lead to a linear response of the diverted current while negative input signals block the diversion of current. A linear calibration fit leads to a diverted current (I_d) of about

$$I_d(U_{\text{in}}) = (0.94 \pm 0.01) \Omega^{-1} \cdot U_{\text{in}} - (0.00 \pm 0.01) \text{ A} \quad (4.10)$$

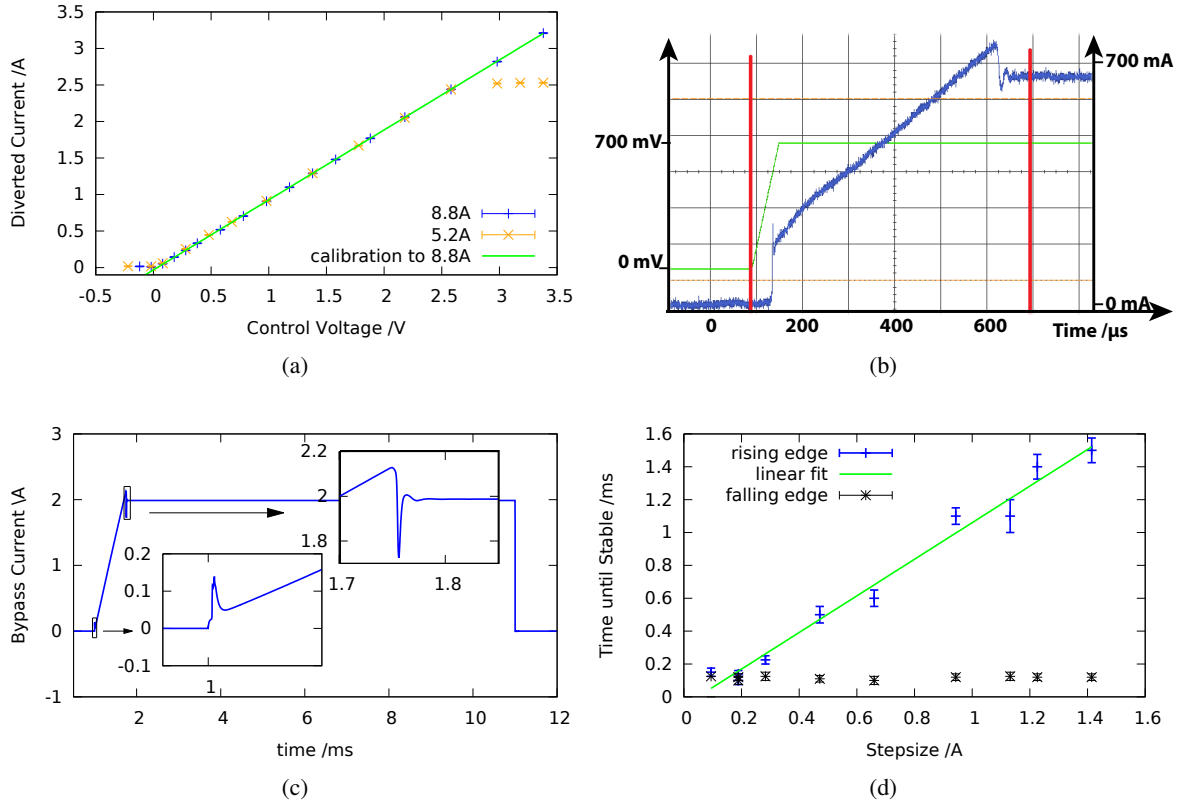


Figure 4.6: **(a)**: Calibration measurements with total currents of 8.8 A and 5.2 A with linear fit to the 8.8 A signal. Until the saturation current the calibration holds independent from I . **(b)**: Response of bypass current (blue) to a step like input signal (green) using the computer controlled circuit. The “Time until Stable” in figure 4.6(d) is marked by the red signs. **(c)**: Simulated step response of the bypass current with few oscillations in LTspice (LTspice IV 4.23h). **(d)**: Measurement of the rise and fall time after a step-like control signal. The measured time starts with the rising input signal and ends when the current is stable (compare figure 4.6(b)). The rise time (blue, with linear fit (green)) is linear to the control signal while the fall time (black) stays constant.

depending on the control voltage (U_{in}). It becomes also clear in figure 4.6(a) that the resistance of the diverting circuit with an open MOSFET is almost equal to R_L since in case of a total current of 5.2 A the diverted current follows exactly the function, which is calibrated using a total current of 8.8 A up to roughly half the total current. The saturation is to be expected due to the ohmic resistance of the diode [32], the MOSFET [27] and the resistance of $R_M = 0.1 \Omega$ in total of $R_{byp} = 0.54 \Omega$. Assuming that the connectors contribute small additional resistances, the ohmic resistances of the coil and the current bypass are equal and explain this saturation current.

Isolated power supply The DC/DC converter (TRACOPOWER TEL-1223 [33]) ensures an electrically isolated power supply. The spikes which are typical for switching power supplies are flattened by an additional capacitance of $2 \mu\text{F}$ on the electrical source-side and a low-pass filter consisting of a 10Ω resistor and a $1 \mu\text{F}$ capacitor at each source ($\pm 15 \text{ V}$) on the ground-free side. Another $5 \mu\text{F}$ connects the two different ground planes for high frequencies including the spikes but disconnects them from high power DC pulses to protect the computer system (see figure 4.5(b)).

Characterisation of the current driver

The current driver's characteristics is investigated using a suddenly changed bypass current using a step like control signal forming a steep ramp (green signal in figure 4.6(b)). The bypass current (blue curve) starts rising after a delay with a step and a following linear rising bypass current. The bypass current stabilises at the final value after an overshooting and short oscillations. The red bar mark the time when the control signal changes until the bypass current is stable again.

Delay time The delay time is not seen in the circuit simulation [34]. During measurements the delay time is at a constant value of about $\Delta t_{\text{delay}} = 50 \mu\text{s}$ in case the control voltage started above zero. When the control voltage started above zero, Δt_{delay} was up to $100 \mu\text{s}$ and depending on the step size what is not further investigated here. Therefore this seems to be a mixture of the transmission bandwidth and the time the last OpAmp needs to raise the gate voltage from the closed MOSFET to a controlled area. The bandwidth of the isolated transmission is limited by the feedback capacitors of 33.47 pF to $f = 10 \text{ kHz}$ [31] what is still larger than the measured delays. The MOSFET completely switches open until it reaches the final value. The first step seems to result from direct response of the snubber-capacitors. This beginning peak was higher using lower R_S in the simulated circuit. The following bypass current is not controlled and follows the law of self inductance[30]. The overshooting at the end of this slope is independent from any changes in the snubber circuits. This is also seen in the simulation (see figure 4.6(c)).

Required switching time The time it takes until a steady state is established after changing the bypass current is important for the duration of a measurement cycle. Figures 4.6(d) and 4.6(b) show this time for a measurement with $I = 8.8 \text{ A}$ starting with the step-like signal until the diverted current is stable. A linear fit to the rise-time (ΔT) gives a relation of

$$\Delta t(\Delta I) = (1.11 \pm 0.06) \text{ ms A}^{-1} \cdot \Delta I - (0.05 \pm 0.04) \text{ ms} \quad (4.11)$$

in dependency of the amount of changed bypass current ΔI . The response time is proportional to the amplitude of the current to be changed at $\Delta t = \sim 1.1 \text{ ms A}^{-1}$. Stopping the diversion of current is stable and much faster and constant at $\Delta t = \sim 120 \mu\text{s}$ since the MOSFET stops the current immediately. Even the simulation show just a sudden stopped current. However, a real experimental sequence requires to ramp up and down in a controlled way for adiabatic transport.

4.5 Thermal analysis

The electrical components dissipate a lot of electrical power which needs do be conducted to the surrounding air to protect the circuit from damage due to overheating. In the following, I will present a calculation to estimate the expected thermal energy dissipated by the MOSFET and the sensing resistor and afterwards a comparison to a temperature measurement using a thermal camera.

4.5.1 Thermal properties

Thermal power The dissipated power P in an electronic device due to guided currents is given by $P = U \cdot I = R \cdot I^2$. The first part is used to calculate the power dissipated by the MOSFET while the second part is an expression to calculate the dissipated power of the sensing resistor. The MOSFET and

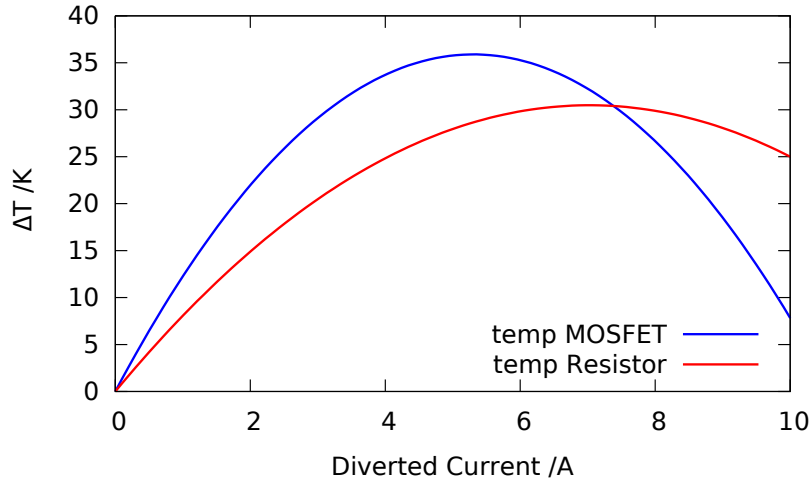


Figure 4.7: Calculated temperature difference between the junction temperature and the surrounding laboratory air temperature. This calculation is based on a total current of 10 A assuming the sensing resistor and the MOSFET to be mounted at the same heat sink and therefore influence each others temperature.

Contributions to	R_{ThM} [K W ⁻¹]	R_{ThR} [K W ⁻¹]
R_{Th} inside component	0,42	2,50
Silicon layer / heat paste	0,33	0,15
Aluminium case	0,03	<0,01
Heat paste	<0,01	0,01
over all resistance	0,78	2,66
Common heat sink to air	1,40	

Table 4.3: Specific R_{Th} of the different layers from the junction area to the common heat sink included in MOSFET's thermal resistance (R_{ThM}) and sensing resistor's dissipated power (R_{ThR}).

the sensing resistor are mounted at the back side of the case to the same heat sink and therefore I assume the back side to have the same temperature for both of them. The summarised power (P_{SUM}) is given by

$$\begin{aligned} P_{SUM} &= P_M + P_R \\ &= I_d R_L (I - I_d), \end{aligned} \quad (4.12)$$

where the gradient coil's resistance is R_L . The different values for thermal resistance (R_{Th}) the MOSFET's dissipated power (P_M), P_R , I_d and the total current I . The temperature difference between the backside casing and the surrounding laboratory air can be calculated using

$$\Delta T = P R_{Th} \quad (4.13)$$

with thermal resistance R_{Th} which is listed for the different layers from the junction area to the common heat sink in table 4.3. To calculate the specific junction temperature difference ΔT one needs to calculate

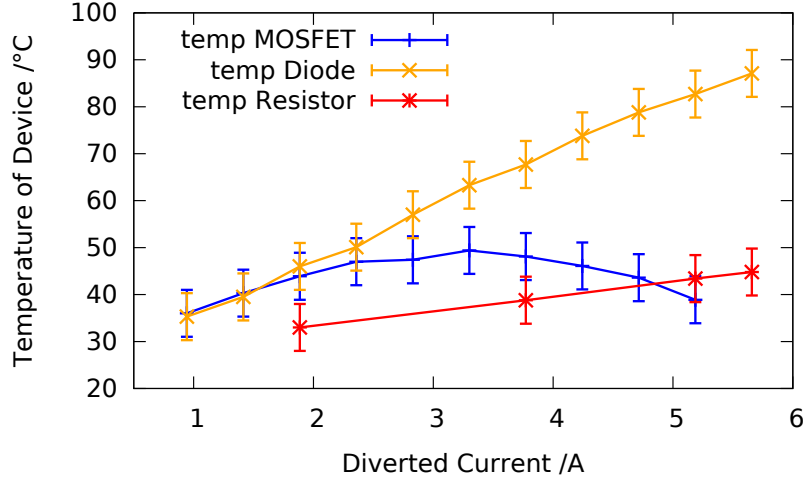


Figure 4.8: Temperature at the hottest point of the measured devices depending on the diverted current in dependency of the diverted current, at a total current of 10.3 A.

in case of the **MOSFET**

$$\begin{aligned} \Delta T_M &= \frac{P_M R_{ThM} + P_{SUM} R_{cool}}{I_d^2 \cdot (-(R_L + R_R) R_{ThM} - R_{cool} R_L) + I_d \cdot I R_L (R_{ThM} + R_{cool})} \\ &= I_d^2 \cdot (-(R_L + R_R) R_{ThM} - R_{cool} R_L) + I_d \cdot I R_L (R_{ThM} + R_{cool}) \end{aligned} \quad (4.14)$$

and in case of the sensing resistor

$$\begin{aligned} \Delta T_R &= \frac{P_R R_{ThR} + P_{SUM} R_{cool}}{I_d^2 \cdot (R_R R_{ThR} - R_L R_{cool}) + I_d \cdot I R_L R_{cool}} \\ &= I_d^2 \cdot (R_R R_{ThR} - R_L R_{cool}) + I_d \cdot I R_L R_{cool} \end{aligned} \quad (4.15)$$

using P_M , R_{ThM} , the thermal resistance of the common heat sink (R_{cool}) and R_{ThR} . Figure 4.7 shows the solution for equations 4.14 and 4.15 in dependency of the diverted current I_d at a total current of $I = 10$ A. The case temperature of the **MOSFET**, which is a marker of its power dissipation, first increases due to the bigger amount of current but decreases after a maximum because the R_M is nearly negligible in case the **MOSFET** completely opens. The sensing resistor's temperature is linked to the **MOSFET**'s temperature since they are mounted close to each other. The sensing resistor's temperature seems to be dominated by the heat of the **MOSFET**. The resistor in use is very precise [26] within a wide range of temperature, for instance for a range of 50 K the resistance changes by less than 2.5% and subsequently shift the **MOT** by less than $5 \mu\text{m}$. The **MOT** is not that sensitive to the effective position since the laser beams have a larger diameter of $w_{MOT} = 2$ mm with a total **MOT** size of $d_{MOT} = \sim 30 - 50 \mu\text{m}$. For compressing and loading the atoms into the **2D-SDL** it is even less important since a the magnetic field gradient will minimize the displacement by nearly a factor of 4 and additionally the bypass circuit switches off during this experimental sequence. Subsequently it is the fact that the sensing resistor does not need to be heated externally to mount it to a separate heat sink.

4.5.2 Heat dissipation

Observing the temperature with a heat camera (Flir T200) while the circuit runs in steady state confirms the calculated values in the previous section. Figure 4.8 gives the device's temperature in dependency of the

diverted current. The total current in this measurement is 10.3 A. It turned out, that a diode dissipates a lot of power and should be cooled with a bigger heat sink at the outer casing. The MOSFET's temperature did not rise over 50 °C and is lower than the expected temperature difference to the surrounding laboratory air temperature. The measurement resistor's temperature is different to the expected curve in figure 4.7. This shows that already the small distance between these devices is enough to treat them more independently.

Conclusion

The thermal properties of this current diversion circuit are sufficient to load caesium atoms in the MOT and load them into the 2D-SDL. The estimated total current to load the MOT is about 9 A and a little bit below the total current of 10.3 A used in the previous measurements. Further on, the duty cycle to load the MOT during an experiment sequence is ~ 0.05 with a bypass current of about ~ 1 A while this thermal characterisation used a steady diverted current of several A.

4.6 Outlook

Next to mounting the power dissipating diode (see figure 4.9(b)) to a proper heat sink outside of the aluminium casing, further characterisation is required to learn more about the circuits limits. A Bode measurement can give additional information on the controlled operating speed already acquired with the measurement of the rise and fall time of the bypass current with an uncontrolled time in between. The magnetic field is not necessarily in a steady state when the bypass current is. Control measurements using a magnetic flux sensor with a bandwidth above 1 kHz give information about the decay of the limiting eddy currents inside the aluminium band coils. Eddy currents in MOT coils in another experiment in this group are limited by eddy currents within the copper cooling plates to a decay time of about 50 ms [22]. Towards loading the MOT automatically controlled by the computer control requires some debugging in the lab. Loading the MOT from time to time requires a different bypass current. Until now the origin of this issue is not clear, since the control circuit diverts reliable the programmed amount of current. One idea is that it is due to saturation effects of the magnetic shielding yielding an magnetic offset field.

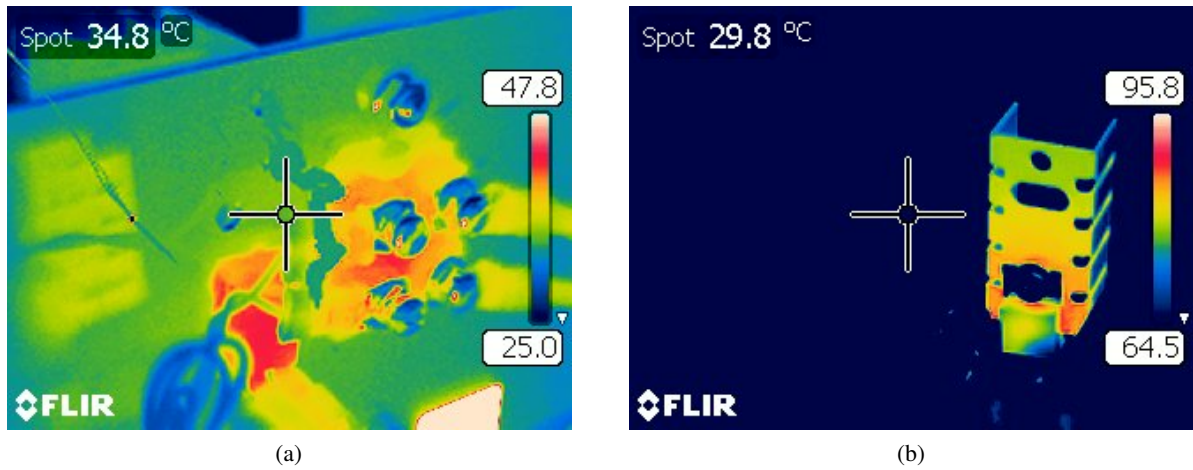


Figure 4.9: Infrared pictures to visualise the thermal behaviour of the electric elements in the current control circuit. In the middle and on the left part are some artefacts due to camera defects. **(a)**: The measurement resistor (right) and the MOSFET (left, partially covered by cables) mounted at the back side of the housing. The heat sink, mounted on the outer side of the aluminium housing is partially visible in the upper part of the image. **(b)**: A diode, where the diverted current is guided through together with its heat sink.

Summary

This thesis deals with theoretical considerations of the three-dimensional confined optical potentials used for state dependent transport in two dimensions. This includes the implementation to perform a transport as well as an analysis of the effective potential depth for the atoms in the different states. The practical part of this thesis consists of the main project to construct a control circuit to operate the magnetic quadrupole field to establish fast loading of atoms from the MOT into the 2D-SDL.

Transport Considerations

Dipole trap potential

The calculated dipole potential for every single optical dipole trap allow to estimate the required trapping laser power and distinguish between a proper cooling or not. The simulation of transport lead to ideas to model a proper transport with respect to optimal acceleration of the atoms. The considered lattice installation shows that a transport performance can lead to a vanishing state dependent lattice even at high laser power due to π -contribution to the state-dependent potential.

Magnetic Elevator

Calibration

The calibration enables the computer system to drive the point of $\vec{B} = 0$ properly. Setting the control value for the diverted current manually allow for capturing caesium atoms out of the background vapour in a MOT 2 mm beneath the high-NA objective and transport them upwards. Implementing the MOT loading into the programmed experiment control cycle requires additional investigation of static magnetic fields in the laboratory since the required current to establish a MOT changed from time to time. This effect is not investigated until now but the origin is assumed in saturation effects in the μ -metal shielding. Probably the implementation of an automatic demagnetisation cycle will solve this problem.

Operation Speed

An increased bypass current is stable after $\Delta t = (1.11 \pm 0.06) \text{ ms A}^{-1}$. This is not necessarily related to the magnetic gradient field in steady state since the metal band coils itself can provide eddy currents requiring a longer damping time. For dimensional reasons the magnetic field cannot be measured at the point of the 2D-SDL. To verify the time until an established constant magnetic field measurements

outside the vacuum glass cell requires a magnetic flux sensor, which is sensitive above 1 kHz. A more sensitive tool would be the direct measurement of coherence with atoms, loaded in the two-dimensional lattice.

Thermal Consideration

The cooling of the MOSFET and the sensing resistor is properly dimensioned. The MOT position at $\vec{B} = 0$ fluctuate by less than $5 \mu\text{m}$ for a temperature difference of $\Delta T = 50 \text{ K}$ due to temperature depending resistance changing. This is as well within the MOT laser beams and does not contribute to the 2D-SDL plane since in this case, there is no bypass current to be measured. Nevertheless mounting the sensing resistor to a separate heat sink further improve its accuracy. The diode reaching high temperatures requires mounting to an external heat sink.

Bibliography

- [1] R. P. Feynman, *Simulating Physics with Computers*, Int. J. Theor. Phys. **21.6/7** (1982) 467 (cit. on p. 1).
- [2] T. Monz et al., *14-Qubit Entanglement: Creation and Coherence*, *Phys. Rev. Lett.* **106** (13 2011) 130506 (cit. on p. 1).
- [3] C. Weitenberg, M. Endres, J. F. Sherson, M. Cheneau, P. Schauß, T. Fukuhara, I. Bloch and S. Kuhr, *Single-spin addressing in an atomic Mott insulator*, *Nature* **471** (2011) 319 (cit. on p. 1).
- [4] A. Schreiber, A. Gábris, P. P. Rohde, K. Laiho, M. Štefaňák, V. Potoček, C. Hamilton, I. Jex and C. Silberhorn, *A 2D Quantum Walk Simulation of Two-Particle Dynamics*, *Science* **336.6077** (2012) 55 (cit. on p. 1).
- [5] A. Schreiber, *Quantum Walks in Time*, PhD thesis: Friedrich-Alexander-Universität Erlangen-Nürnberg, 2013 (cit. on p. 1).
- [6] M. Genske, W. Alt, A. Steffen, A. H. Werner, R. F. Werner, D. Meschede and A. Alberti, *Electric quantum walks with individual atoms*, *Phys. Rev. Lett.* **110** (2013) 190601 (cit. on p. 1).
- [7] S. Brakhane, W. Alt, D. Meschede, C. Robens and A. Alberti, *Ultra-low birefringence dodecagonal vacuum glass cell*, Submitted (2015) (cit. on pp. 1, 3, 6, 7, 16).
- [8] E. L. Raab, M. Prentiss, A. Cable, S. Chu and D. E. Pritchard, *Trapping of Neutral Sodium Atoms with Radiation Pressure*, *Phys. Rev. Lett.* **59** (23 1987) 2631 (cit. on p. 3).
- [9] H. J. Metcalf and P. van der Straten, *Laser Cooling and Trapping*, ed. by R. Berry, J. L. Birman, J. W. Lynn, M. P. Silverman, H. E. Stanley and M. Voloshin, Springer-Verlag, 1999 (cit. on p. 3).
- [10] M. Karski, L. Förster, J. Choi, W. Alt, A. Alberti, A. Widera and D. Meschede, *Direct Observation and Analysis of Spin-Dependent Transport of Single Atoms in a 1D Optical Lattice*, *J. Korean Phys. Soc.* **59.4** (2011) 2947 (cit. on pp. 3–5, 7).
- [11] D. Döring, *Ein Experiment zum zustandsabhängigen Transport einzelner Atome*, Diplomarbeit, 2007 (cit. on pp. 4, 5, 7, 9).
- [12] R. Grimm, M. Weidemüller and Y. B. Ovchinnikov, “Optical Dipole Traps for Neutral Atoms”, ed. by B. Bederson and H. Walther, vol. 42, *Advances In Atomic, Molecular, and Optical Physics*, Academic Press, 2000 95 (cit. on pp. 3, 9).
- [13] C. Robens, private communication, 2015 (cit. on p. 5).
- [14] A. Härter, *Ein Aufbau zur kohärenten Manipulation und zum zustandsabhängigen Transport einzelner Atome*, MA thesis, 2007 (cit. on p. 4).

- [15] F. Kleißler, *Assembly and Characterization of a High Numerical Aperture Microscope for Single Atoms*, MA thesis, 2014 (cit. on pp. 6, 9).
- [16] S. Brakhane, private communication, 2015 (cit. on pp. 6, 12, 16).
- [17] C. Robens, “A high-numerical-aperture microscope objective for optical imaging an addressing of cold atoms”, 2014 (cit. on pp. 7, 16).
- [18] D. A. Steck, *Cesium D Line Data* (2010) (cit. on p. 7).
- [19] M. Greiner, I. Bloch, T. W. Hänsch and T. Esslinger, *Magnetic transport of trapped cold atoms over a large distance*, *Phys. Rev. A* **63** (3 2001) 031401 (cit. on p. 7).
- [20] C. Weitenberg, *Single-Atom Resolved Imaging and Manipulation in an Atomic Mott Insulator*, PhD thesis: Ludwig-Maximilians-Universität München, 2011 (cit. on p. 8).
- [21] F. Bloch, *Nuclear Induction*, *Phys. Rev.* **70** (7-8 1946) 460 (cit. on p. 8).
- [22] W. Alt, *Optical control of single neutral atoms*, PhD thesis: University Bonn, 2004 (cit. on pp. 9, 19, 27).
- [23] I. Wolfram Research, *Mathematica*, Version 10.1, Champaign, Illinois: Wolfram Research, Inc., 2015 (cit. on p. 10).
- [24] H. Wheeler, *Simple Inductance Formulas for Radio Coils*, *Radio Engineers, Proceedings of the Institute of* **16.10** (1928) 1398, ISSN: 0731-5996 (cit. on pp. 17, 19).
- [25] P. Horowitz and W. Hill, *The Art of Electronics*, Second Edition, Cambridge University Press, 1994 (cit. on p. 17).
- [26] *ISA-PLAN - Präzisionswiderstände*, RTO-B 0R100, Isabellenhütte Heusler GmbH & Co. KG, Eibacher Weg 3-5, D-35683 Dillenburg (cit. on pp. 19, 26).
- [27] *Power MOSFET*, IXTH 88N30P, IXYS, 2005 (cit. on pp. 19, 23).
- [28] *270-MHz High-Speed Amplifier*, THS 4001, Texas Instruments, Post Office Box 655303, Dallas, Texas 75265, 1997 (cit. on p. 19).
- [29] U. Tietze, c. Schenk and E. Gamm, *Halbleiter-Schaltungstechnik*, 12. Auflage, Berlin: Springer-Verlag, 2002, ISBN: 3-540-42849-6 (cit. on p. 19).
- [30] W. Demtröder, *Experimentalphysik 2: Elektrizität und Optik*, Experimentalphysik / Wolfgang Demtröder, Springer Berlin Heidelberg, 2007, ISBN: 9783540337959 (cit. on pp. 20, 24).
- [31] *High-Linearity Analog Optocouplers*, HCNR 201, Avago Technologies, 2014 (cit. on pp. 21, 22, 24).
- [32] *Power Rectifier*, MUR1520/D, ON Semiconductor (cit. on p. 23).
- [33] *DC/DC Converters*, TEL2-1223, Traco power, Jenatschstraße 1, CH-8002 Zürich, 2009 (cit. on p. 23).
- [34] M. Engelhardt, *LTspice 4.23h*, 2015 (cit. on p. 24).

Additional explanations / data

A.1 Inductivity using *LR*-circuit

R_{res} / Ω	exponent / s^{-1}	L / mH
75.08 ± 0.74	$12\,121.80 \pm 51.00$	6.19 ± 0.07
50.39 ± 0.50	$8\,444.50 \pm 38.14$	5.97 ± 0.06
70.64 ± 0.70	$11\,682.90 \pm 28.26$	6.05 ± 0.06
38.14 ± 0.38	$6\,564.27 \pm 12.19$	5.81 ± 0.06
27.91 ± 10.50	$4\,642.05 \pm 5.86$	6.01 ± 2.26
9.456 ± 0.150	$1\,525.11 \pm 0.01$	6.20 ± 0.98
	Average	6.04 ± 0.82

Table A.1: Data from single measurements to calculate the top coils inductance using a *LR*-circuit.

R_{res} / Ω	exponent / s^{-1}	L / mH
75.08 ± 0.74	$13\,905.90 \pm 79.45$	5.40 ± 0.05
75.08 ± 0.74	$14\,018.20 \pm 90.21$	5.36 ± 0.05
38.14 ± 0.38	$6\,661.45 \pm 26.59$	5.73 ± 0.06
38.14 ± 0.38	$6\,512.29 \pm 23.32$	5.86 ± 0.06
70.64 ± 0.70	$11\,037.60 \pm 36.70$	6.34 ± 0.06
70.64 ± 0.70	$11\,020.80 \pm 32.37$	6.41 ± 0.06
60.64 ± 10.50	$9\,329.12 \pm 22.50$	6.50 ± 1.13
60.64 ± 10.50	$9\,291.79 \pm 22.71$	6.53 ± 1.13
	Average	6.02 ± 0.46

Table A.2: Data from single measurements to calculate the bottom coils inductance using a *LR*-circuit.

A.2 Inductivity using *LC*-circuit

ω / s^{-1}	$C / \mu\text{F}$	L / mH
$1\,240.45 \pm 0.25$	100 ± 20	6.50 ± 1.30
$1\,269.25 \pm 1.02$	100 ± 20	6.21 ± 1.24
$1\,262.00 \pm 0.03$	100 ± 20	6.28 ± 1.26
$1\,261.00 \pm 0.02$	100 ± 20	6.29 ± 1.26
$1\,262.34 \pm 0.12$	100 ± 20	6.28 ± 1.26
$1\,217.820 \pm 0.003$	100 ± 20	6.74 ± 1.35
	Average	6.38 ± 0.18

Table A.3: Data from single measurements to calculate the top coils inductance using a *LC*-circuit

ω / s^{-1}	$C / \mu\text{F}$	L / mH
$1\,228.82 \pm 0.87$	100 ± 20	6.62 ± 1.32
$1\,242.65 \pm 0.79$	100 ± 20	6.48 ± 1.30
$1\,241.54 \pm 0.85$	100 ± 20	6.49 ± 1.30
$1\,240.23 \pm 0.11$	100 ± 20	6.50 ± 1.30
$1\,240.29 \pm 0.11$	100 ± 20	6.50 ± 1.30
$1\,236.94 \pm 0.19$	100 ± 20	6.54 ± 1.30
$1\,236.09 \pm 0.14$	100 ± 20	6.54 ± 1.31
$1\,240.88 \pm 0.12$	100 ± 20	6.49 ± 1.30
$1\,242.04 \pm 0.15$	100 ± 20	6.48 ± 1.30
	Average	6.54 ± 0.08

Table A.4: Data from single measurements to calculate the bottom coils inductance using a *LC*-circuit

A.3 Capacity using LC-circuit

ω / s^{-1}	C / nF
$327\,739.0 \pm 644.8$	1.50 ± 0.20

Table A.5: Data from a single measurements to calculate the top coils capacitance using a LC-circuit.

ω / s^{-1}	C / nF
$350\,506.0 \pm 168.5$	1.30 ± 0.10
$354\,055.0 \pm 179.5$	1.27 ± 0.10
Average	1.28 ± 0.01

Table A.6: Data from single measurements to calculate the top coils capacitance using a LC-circuit

List of Figures

2.1	Position dependent force of a magneto-optical trap	4
2.2	State dependent lattice	5
2.3	Creation of 2D-SDL by two independent 1D-SDL	5
2.4	Sketch of vacuum system	6
2.5	Selection of atoms in the focus depth and vertical confinement	8
3.1	Simulated one-dimensional trap potential	10
3.2	Laser configuration and displacement for one-dimensional state dependent transport	11
3.3	Potential depth in an 1D-SDL for the qubit states $ \uparrow\rangle, \downarrow\rangle$	12
3.4	Improved transport schematics	13
4.1	Schematic overview of science chamber	16
4.2	Circuit for characterising the gradient coils and related data plots	18
4.3	Basic idea of current diversion	20
4.4	Current diversion circuit including all components	21
4.5	Galvanic isolated circuits	22
4.6	Calibration and step response analysis	23
4.7	Calculated device temperature in use for 10 A	25
4.8	Power dissipation of the electrical elements for $I = 10.3$ A	26
4.9	Heat pictures of electrical elements	28

List of Tables

3.1	Comparison of transport schemes	12
4.1	Dimensions and properties of the used magnetic coils	16
4.2	Gradient coil properties	19
4.3	Thermal resistances	25
A.1	Data: Inductance of top coil (LR-circuit)	33
A.2	Data: Inductance of bottom coil (LR-circuit)	33
A.3	Data: Inductance of top coil (LC-circuit)	34
A.4	Data: Inductance of bottom coil (LC-circuit)	34
A.5	Data: Capacitance of top coil (LC-circuit)	35
A.6	Data: Capacitance of bottom coil (LC-circuit)	35

Acronyms

- \vec{E}_{circ} electric field vector in circular basis. [10](#)
- λ_{m} system specific wavelength. [4](#), [7](#)
- C_{L} gradient coil's capacity. [16](#), [17](#), [18](#)
- C_{ext} external capacitance. [17](#), [18](#)
- I_{d} diverted current. [22](#), [25](#)
- I_{max} intensity maximum. [9](#)
- L_{L} gradient coil's inductivity. [16](#), [17](#), [18](#)
- P_{M} MOSFET's dissipated power. [25](#), [26](#)
- P_{R} sensing resistor's dissipated power. [24](#), [25](#)
- P_{SUM} summarised power. [24](#), [25](#), [26](#)
- R_{L} gradient coil's resistance. [16](#), [17](#), [18](#), [22](#), [25](#)
- R_{M} sensing resistance. [19](#), [21](#), [22](#), [26](#)
- R_{cool} thermal resistance of the common heat sink. [26](#)
- R_{ThM} MOSFET's thermal resistance. [25](#), [26](#)
- R_{ThR} sensing resistor's dissipated power. [25](#), [26](#)
- R_{Th} thermal resistance. [25](#)
- U_{L} voltage across one gradient coil. [17](#)
- U_{in} control voltage. [22](#)
- U_{max} maximal potential depth. [9](#)
- 1D-SDL** one-dimensional state-dependent optical lattice. [10](#), [11](#), [37](#)
- 2D-SDL** two-dimensional state-dependent optical lattice. [3](#), [7](#), [9](#), [11](#), [15](#), [26](#), [27](#), [29](#), [30](#), [37](#)
- AOM** acousto-optic modulator. [4](#), [11](#)
- DC** direct current. [4](#), [16](#), [23](#)

DQSIM discrete quantum simulation. [3](#), [5](#), [43](#)

EMCCD electron multiplying charge-coupled device. [7](#)

LED light emitting diode. [21](#)

MOSFET metal–oxide–semiconductor field-effect transistor. [19](#), [22](#), [24](#), [25](#), [26](#), [30](#)

MOT magneto-optical trap. [3](#), [7](#), [15](#), [16](#), [19](#), [26](#), [27](#), [29](#), [30](#)

NA numerical aperture. [3](#), [6](#), [7](#), [15](#), [16](#), [29](#)

NEG-pump non-evaporable getter pump. [6](#)

OpAmp operation amplifier. [19](#), [21](#), [24](#)

UHV ultra-high vacuum. [3](#), [15](#)

Acknowledgements

Zum Abschluss des praktischen Teils meiner Masterarbeit möchte ich **Danke!** sagen.

Danke ...

- ... Professor Meschede, für die sehr spannende Zeit den Aufbau des [DQSIM](#)-Experimentes mit zu erleben und zu gestalten.
- ... Frau Dr. Soergel, für die Übernahme des Zweitgutachtens.
- ... Dr. Andrea Alberti und Dr. Wolfgang Alt, für die vielen hilfreichen Diskussionen.
- ... Stefan Brakhane für die gesamte Unterstützung und Betreuung während meiner Zeit in der AG Quantentechnologie, deren detaillierte Erwähnung nicht möglich ist.
- ... Carsten Robens für die Unterstützung bei der Laborarbeit und praktische Hinweise für Vorträge und Niedergeschriebenes.
- ... Gautam für die Motivation auf der Zielgeraden.
- ... für die Unterstützung zwischendurch bei Geol, Tobi, Nathalie, Muhammad, Florian, Josè.
- ... den Unterstützern im Hintergrund bei organisatorischen Fragen: Anneliese, Fien und Dietmar.
- ... allen, die mich auch abseits der Physik unterstützt und motiviert haben ...

I hereby declare that this thesis was formulated by myself and that no sources or tools other than those cited were used.

Bonn,
Date

.....
Signature